



Cite this: *J. Mater. Chem. A*, 2016, **4**, 15207  
15207

## Vanadium-free colusites $\text{Cu}_{26}\text{A}_2\text{Sn}_6\text{S}_{32}$ (A = Nb, Ta) for environmentally friendly thermoelectrics†

Yuta Kikuchi,<sup>a</sup> Yohan Bouyrie,<sup>a</sup> Michihiro Ohta,<sup>\*a</sup> Koichiro Suekuni,<sup>b</sup> Makoto Aihara<sup>a</sup> and Toshiro Takabatake<sup>cd</sup>

The thermoelectric properties of colusites  $\text{Cu}_{26}\text{A}_2\text{Sn}_6\text{S}_{32}$  with A = V, Nb, and Ta have been investigated on high-density sintered compacts over the temperature range of 300–670 K. The ingots melted in evacuated and sealed quartz tubes were found to be composed of two colusite phases with slightly different lattice parameters. The successive hot-pressing converted the two-phase samples to single-phase ones of high density. Scanning electron microscopic analysis revealed the presence of CuS- and  $\text{Cu}_2\text{S}$ -based secondary phases in only the sintered compact with A = Ta. For A = V, Nb, and Ta samples, the heavy hole effective mass of  $3m_0$ – $4m_0$  ( $m_0$ : free electron mass) caused a high Seebeck coefficient, leading to a high thermoelectric power factor of 0.6–0.7 mW K<sup>–2</sup> m<sup>–1</sup> at 660 K. The electrical resistivity and lattice thermal conductivity for the A = Ta sample are lower than those for A = V and A = Nb samples, because the secondary phases in the A = Ta sample provide charge carriers and scatter effectively the phonons. As a result, a *ZT* of 0.8 at 670 K is achieved for the A = Ta system.

Received 14th July 2016  
Accepted 29th August 2016  
DOI: 10.1039/c6ta05945g  
[www.rsc.org/MaterialsA](http://www.rsc.org/MaterialsA)

## 1. Introduction

In aiming at mitigating climate change, thermal management should be improved in various fields such as vehicles, industrial processes, and fossil fuel combustion, because more than 50% of the primary energy consumed is wasted in the form of heat.<sup>1</sup> Solid-state devices based on thermoelectrics can directly generate electrical energy from the waste heat, and thus provide a new strategy for reducing and managing energy consumption.<sup>2–5</sup>

For a thermoelectric device, the efficiency in converting thermal energy to electrical energy depends on the thermoelectric figure of merit *ZT* of the material, described as:

$$ZT = \frac{S^2}{\rho(\kappa_{\text{el}} + \kappa_{\text{lat}})} T \quad (1)$$

where *S* is the Seebeck coefficient,  $\rho$  is the electrical resistivity,  $\kappa_{\text{el}}$  is the electronic thermal conductivity,  $\kappa_{\text{lat}}$  is the lattice thermal conductivity, and *T* is the absolute temperature. The *ZT*

is improved through the enhancement of thermoelectric power factor  $S^2/\rho$  and reduction of  $\kappa_{\text{lat}}$ . The potential materials for high performance thermoelectrics are  $\text{Bi}_2\text{Te}_3$  for near-room-temperature applications and  $\text{PbTe}$  for intermediate-temperature ( $\sim$ 700 K) applications.<sup>6</sup> In particular, the *ZT* of  $\text{PbTe}$ -based materials has been dramatically enhanced by nanostructuring.<sup>7–15</sup> Recently, high *ZT* values were also reported for new class thermoelectric materials such as  $\text{SnSe}$ <sup>16,17</sup> and  $\text{MgAgSb}$ .<sup>18</sup>

Industrial application of thermoelectric devices requires high-*ZT* materials composed of less-toxic and cost effective elements. This requirement is, however, not satisfied for conventional thermoelectric materials such as  $\text{Bi}_2\text{Te}_3$  and  $\text{PbTe}$ , because they are composed of toxic (Pb) and expensive (Te) elements. On the other hand, copper (Cu) and sulfur (S) are earth abundant and less-toxic elements; therefore, copper-containing sulfides have been intensively studied in the past several years.<sup>19</sup>

Binary copper sulfides  $\text{Cu}_{1.97}\text{S}$  have been reported to have *ZT* over  $\sim$ 1.9 at 973 K.<sup>20,21</sup> In these systems, liquid-like Cu ions travel freely within the sulfur sublattice, reducing the  $\kappa_{\text{lat}}$  to 0.6 W K<sup>–1</sup> m<sup>–1</sup>. However, this Cu migration drives the physical degradation of materials.<sup>22</sup> Tetrahedrites  $\text{Cu}_{12-x}\text{Tr}_x\text{Sb}_4\text{S}_{13}$  ( $\text{Tr} = \text{Mn, Fe, Co, Ni, and Zn}$ ) have been demonstrated to possess promising thermoelectric properties over the intermediate temperature range of 600–700 K. The high p-type *ZT* ( $\sim$ 1.0 at 700 K for  $\text{Cu}_{10.5}\text{Ni}_{1.0}\text{Zn}_{0.5}\text{Sb}_4\text{S}_{13}$ ) arises from the combination of a degenerate semiconducting-like band structure and an extremely low  $\kappa_{\text{lat}}$  ( $\sim$ 0.4 W K<sup>–1</sup> m<sup>–1</sup> at 700 K for  $\text{Cu}_{10.5}\text{Ni}_{1.0}\text{Zn}_{0.5}\text{Sb}_4\text{S}_{13}$ ).<sup>23–31</sup> However, tetrahedrites contain a somewhat toxic element (Sb) which prevents them from industrial applications.

<sup>a</sup>Research Institute for Energy Conservation, National Institute of Advanced Industrial Science and Technology (AIST), Tsukuba, Ibaraki 305-8568, Japan. E-mail: ohta.michihiro@aist.go.jp

<sup>b</sup>Department of Applied Science for Electronics and Materials, Interdisciplinary Graduate School of Engineering Sciences, Kyushu University, Kasuga, Fukuoka 816-8580, Japan

<sup>c</sup>Department of Quantum Matter, Graduate School of Advanced Sciences of Matter, Hiroshima University, Higashi-Hiroshima, Hiroshima 739-8530, Japan

<sup>d</sup>Institute for Advanced Materials Research, Hiroshima University, Higashi-Hiroshima, Hiroshima 739-8530, Japan

† Electronic supplementary information (ESI) available. See DOI: 10.1039/c6ta05945g



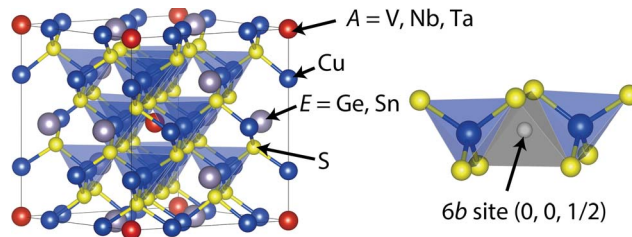


Fig. 1 Crystal structure of colusites  $\text{Cu}_{26}\text{A}_2\text{Sn}_6\text{S}_{32}$  ( $\text{A} = \text{V}, \text{Nb}, \text{Ta}$ ).<sup>36,37</sup> The crystal structure is simple cubic (space group:  $\bar{P}43n$ ) containing 66 atoms in a unit cell. The empty 6b site is located between two  $[\text{Cu}_4]$  tetrahedra.

$\text{Cu}_{26}\text{V}_2\text{E}_6\text{S}_{32}$  ( $\text{E} = \text{Ge}, \text{Sn}$ ) are a family of colusites without Sb, therefore highly promising for practical thermoelectric devices operating in the intermediate temperature range of 600–700 K.<sup>31–35</sup> The crystal structure of colusites is shown in Fig. 1. The unit cell is composed of 66 atoms and belongs to a cubic system with a  $\bar{P}43n$  space group.<sup>35–37</sup> In the crystal structure, there are large void spaces at interstitial sites, such as 6b (0, 0, 1/2). It has been reported that the density of states (DOS) calculations show unoccupied states in the valence band above the fermi level, allowing p-type conduction.<sup>32,33</sup> This electron-deficient character is consistent with the electron count for formal valences such as  $\text{Cu}^+(3\text{d}^{10})$ ,  $\text{V}^{5+}(3\text{d}^0)$ ,  $\text{E}^{4+}$ , and  $\text{S}^{2-}$ .<sup>32,33</sup> We have demonstrated relatively high p-type  $ZT$  values (0.6–0.7 at 663 K) owing to the low  $\kappa_{\text{lat}}$  ( $\sim 0.5 \text{ W K}^{-1} \text{ m}^{-1}$  at 300–670 K). The low  $\kappa_{\text{lat}}$  is attributed to the large number of atoms in the simple cubic crystal structure. Moreover, the electronic band structure calculation revealed that the high power factor of  $\sim 0.6 \text{ mW K}^{-2} \text{ m}^{-1}$  at 663 K originates from the Cu-3d and S-3p hybridized orbitals close to the Fermi level.<sup>32,33</sup>

Although colusites could pave the way for environmentally friendly and cost-effective thermoelectric generation, there are concerns regarding the oxidation of V in the production processes and practical use because V-oxides are toxic.<sup>38,39</sup> Therefore, an attempt was made to substitute less toxic elements Nb and Ta for V in colusites. Isoelectronic elements V, Nb and Ta are expected to lead to a similar electronic band structure in the colosite system; therefore, the value of  $S^2/\rho$  for  $\text{Cu}_{26}\text{Nb}_2\text{Sn}_6\text{S}_{32}$  and  $\text{Cu}_{26}\text{Ta}_2\text{Sn}_6\text{S}_{32}$  could be high, like that for  $\text{Cu}_{26}\text{V}_2\text{Sn}_6\text{S}_{32}$ . Furthermore, the large number of atoms in the unit cell of  $\text{Cu}_{26}\text{Nb}_2\text{Sn}_6\text{S}_{32}$  and  $\text{Cu}_{26}\text{Ta}_2\text{Sn}_6\text{S}_{32}$  would yield a low  $\kappa_{\text{lat}}$ . Bearing this in mind, we have synthesized  $\text{Cu}_{26}\text{A}_2\text{Sn}_6\text{S}_{32}$  ( $\text{A} = \text{V}, \text{Nb}, \text{Ta}$ ) and compared their thermoelectric properties.

## 2. Experimental section

### 2.1 Synthesis and sintering

Elemental copper (Cu; 99.99%), vanadium (V; 99.9%), niobium (Nb; 99.9%), tantalum (Ta; 99.9%), tin (Sn; 99.9999%), and sulfur (S; 99.9999%) supplied from Kojundo Chemical Laboratory were used as starting materials without further purification. These elements were mixed in the stoichiometric ratio of  $\text{Cu}_{26}\text{A}_2\text{Sn}_6\text{S}_{32}$  ( $\text{A} = \text{V}, \text{Nb}, \text{Ta}$ ). For example, 1.321 g of Cu, 0.289 g of Ta, 0.569 g of Sn, and 0.820 g of S were used to prepare 3 g of

$\text{Cu}_{26}\text{Ta}_2\text{Sn}_6\text{S}_{32}$ . A mixture of approximately 3 g was loaded into fused quartz tubes of 12 mm outer diameter  $\times$  8 mm inner diameter. The tubes were evacuated to a pressure of  $\sim 5 \times 10^{-3}$  Pa and then flame-sealed. The mixtures were heated to 1323 K for 60 h, held at 1323 K for 12 h, cooled to 673 K in 19 h, and then to room temperature over 5 h.

The obtained ingots of  $\text{Cu}_{26}\text{A}_2\text{Sn}_6\text{S}_{32}$  were hand-ground into powders, which were placed into graphite dies with 10 or 15 mm-inner diameter for hot pressing. The graphite die was inserted into a hot-press furnace (FUT-17000, TOKYO VACUUM). Sintering was performed at 1023 K for 1 h under 70 MPa uniaxial pressure in an Ar gas flow atmosphere. The heating and cooling rates were  $10 \text{ K min}^{-1}$  and  $20 \text{ K min}^{-1}$ , respectively. The density of the sintered compacts was determined using the gas pycnometer method (AccuPyc II 1340, Micromeritics). The sintered compacts of 15 mm diameter were cut into rods of  $\sim 2 \times \sim 2 \times \sim 7$  mm for the measurements of the Seebeck coefficient and electrical resistivity, and squares of  $\sim 10 \times \sim 10 \times \sim 2$  mm for thermal diffusivity measurements. The sintered compacts of 10 mm diameter were cut into plates of  $\sim 5 \times \sim 5 \times \sim 0.2$  mm for Hall measurements.

### 2.2 Powder X-ray diffraction and scanning electron microscopy

Crystal structures of the as-prepared ingots and sintered compacts were examined by powder X-ray diffractometry (XRD; MiniFlex600, Rigaku) with Cu  $\text{K}\alpha$  radiation over the  $2\theta$  range 10–100° at room temperature. The powder XRD patterns were refined by the Le Bail method using the JANA2006<sup>40</sup> to calculate the lattice parameters. The crystal structures were drawn with the VESTA software.<sup>41</sup>

The microstructures and chemical compositions of the sintered compacts were investigated by scanning electron microscopy (SEM; 15 kV, Miniscope TM3030Plus, Hitachi High-Technologies) with energy dispersive X-ray spectroscopy (EDX; Quantax70, Bruker).

### 2.3 Thermogravimetric analysis

The thermogravimetry curves of the as-prepared ingots and sintered compacts were obtained using a DTG-60 (Shimadzu). The powders of 5 mg mass were put in a boron nitride crucible and heated to 1023 K under an Ar gas flow atmosphere (100 ml min<sup>-1</sup>) at a rate of  $5 \text{ K min}^{-1}$ . The  $\alpha\text{-Al}_2\text{O}_3$  powder was used as a reference.

### 2.4 Electrical transport measurement

The Seebeck coefficient  $S$  and electrical resistivity  $\rho$  of the sintered compacts were simultaneously measured using temperature-differential and four-probe methods, respectively, under a He atmosphere over the temperature range of 300–670 K (ZEM-3, ADVANCE RIKO). The values of  $S$  and  $\rho$  were reproducible over heating and cooling cycles for all samples. The relative uncertainty of the measurements was estimated to be 5%.

The Hall coefficient  $R_H$  was measured at room temperature by the Van der Pauw method with a home-built system under a magnetic field of 2.3 tesla. The Cu contact wires were attached to the sintered samples using In-rich In–Ga paste.



## 2.5 Thermal transport measurement

The total thermal conductivity  $\kappa_{\text{total}}$  of the sintered compacts was calculated from the density ( $d$ ), heat capacity  $C_p$ , and thermal diffusivity  $D$  using the expression  $\kappa_{\text{total}} = dC_pD$ . The thermal diffusivity was directly measured and the heat capacity was indirectly derived using a standard sample (Pyroceram 9606, Netzsch) using the laser flash method (LFA 457 MicroFlash, Netzsch) under an Ar gas flow atmosphere at 100 ml min<sup>-1</sup> over the temperature range of 300–670 K. Graphite spray coating was applied on the sample surface in order to improve the emission and absorption properties. The heat capacity and thermal diffusivity were measured over heating and cooling cycles. The heat capacity and thermal diffusivity are provided in Fig. S1 in the ESI.† The relative uncertainty of the thermal conductivity is estimated to be smaller than 8% from the uncertainties of  $d$ ,  $C_p$ , and  $D$ . Thus, the combined relative uncertainty for the calculation of  $ZT$  is approximately 12%.

## 3. Results and discussion

### 3.1 Synthesis and sintering

Fig. 2(a) shows the powder X-ray diffraction (XRD) patterns of the as-prepared ingots of  $\text{Cu}_{26}\text{A}_2\text{Sn}_6\text{S}_{32}$  ( $\text{A} = \text{V}, \text{Nb}, \text{Ta}$ ) over the  $2\theta$  range of 10–100° at room temperature. Most of the reflections are those of the cubic colusite-type structure with a  $P\bar{4}3n$  space group,<sup>36,37</sup> while weak peaks due to impurities are observed. Moreover, the main peaks are split as shown in the inset (see Fig. 2(b)), which cannot be accounted for by using the different wavelengths of  $\text{Cu K}\alpha_1$  and  $\text{K}\alpha_2$ . In our previous work, the scanning electron microscopy (SEM) examination with wavelength dispersive X-ray spectroscopy (SEM-WDX) has revealed that the sintered compact with  $\text{A} = \text{V}$  consists of two colusite phases with slightly different chemical compositions (Sn poor and Sn rich phases).<sup>32–34</sup> Moreover, the Sn-poor and Sn rich colusite phases have been formed in natural colusites.<sup>36</sup> In our as-prepared samples, the splitting of the main peaks on the XRD patterns is probably due to the presence of two colusite phases. This experimental observation likely originates from an exsolution phenomenon.<sup>35</sup>

Fig. 3(a) and S2 in the ESI† show the XRD patterns of the sintered compacts of  $\text{Cu}_{26}\text{A}_2\text{Sn}_6\text{S}_{32}$  ( $\text{A} = \text{V}, \text{Nb}, \text{Ta}$ ) with simulated ones over the  $2\theta$  range of 10–60° and  $2\theta$  range of 10–100°, respectively, at room temperature. Unlike the as-prepared ingots (Fig. 2), no impurity peaks are observed in the sintered compacts within the detection limits of the XRD. Furthermore, the XRD peak splitting disappears as shown in Fig. 3(b). In our previous study, XRD peak splitting remained in the  $\text{A} = \text{V}$  system after the sintering with a holding time of 5 min to 10 min.<sup>32–34</sup> The longer holding time (1 h) in the sintering process causes an annealing effect, promoting the change from two colusite phases to a single colusite phase.

The refined lattice parameters of the two colusite phases for the as-prepared ingots are denoted as  $a_1$  and  $a_2$  (with  $a_1 > a_2$ ) and that of the single colusite phase for the sintered compacts is denoted as  $a$ . The  $a_1$ ,  $a_2$  and  $a$  are listed in Table 1 for all  $\text{A} = \text{V}$ ,  $\text{Nb}$ , and  $\text{Ta}$  systems. The  $a_1$  is  $\sim 0.4\%$  larger than the  $a_2$ ; for example, the  $a_1$  and  $a_2$  of  $\text{Cu}_{26}\text{Ta}_2\text{Sn}_6\text{S}_{32}$  are 1.0865 nm and 1.0827 nm, respectively. The  $a$  is slightly larger than  $a_1$  for all systems; for example, the  $a$  of the  $\text{A} = \text{Ta}$  system (1.0885 nm) is  $\sim 0.2\%$  larger than  $a_1$  (1.0865 nm).

In the thermogravimetry (TG) curve for the as-prepared ingots, the weight drops sharply over the temperature of 600–700 K in an Ar flow atmosphere (Fig. 4(a)). The weight reductions are likely due to the evaporation of a part of sulfur, which has the lowest boiling point of 718 K among all the constituent elements. This result implies that the metal content of sintered compacts is larger than the stoichiometric value. This is in fact supported by the SEM-EDX as discussed below. No weight loss was detected in the TG curves up to 750 K for all sintered compacts, as shown in Fig. 4(b).

The SEM back scattered electron (BSE) images of the polished surface of the sintered compacts of  $\text{Cu}_{26}\text{A}_2\text{Sn}_6\text{S}_{32}$  ( $\text{A} = \text{V}, \text{Nb}, \text{Ta}$ ) are shown in Fig. 5. The SEM-EDX investigations reveal a high homogeneity for  $\text{A} = \text{Nb}$  and  $\text{V}$  but the presence of secondary phases for the  $\text{A} = \text{Ta}$  sintered compact. For the latter, microscale  $\text{CuS}$ - and  $\text{Cu}_2\text{S}$ -based secondary phases were identified, whose actual compositions are listed in Table S1 in the ESI.†

For the sintered compacts, the nominal composition, measured density, and calculated density are summarized in

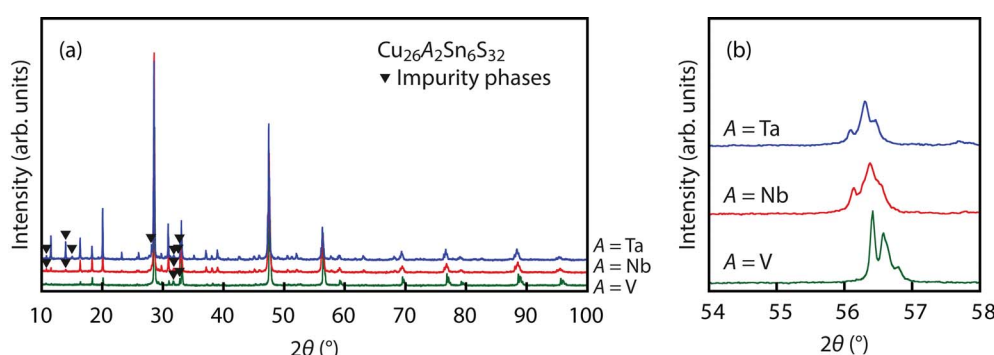


Fig. 2 (a) Powder X-ray diffraction (XRD) patterns for the as-prepared ingots of  $\text{Cu}_{26}\text{A}_2\text{Sn}_6\text{S}_{32}$  ( $\text{A} = \text{V}, \text{Nb}, \text{Ta}$ ) over the  $2\theta$  range of 10–100°. (b) The inset shows the 622 peaks on the expanded scale.



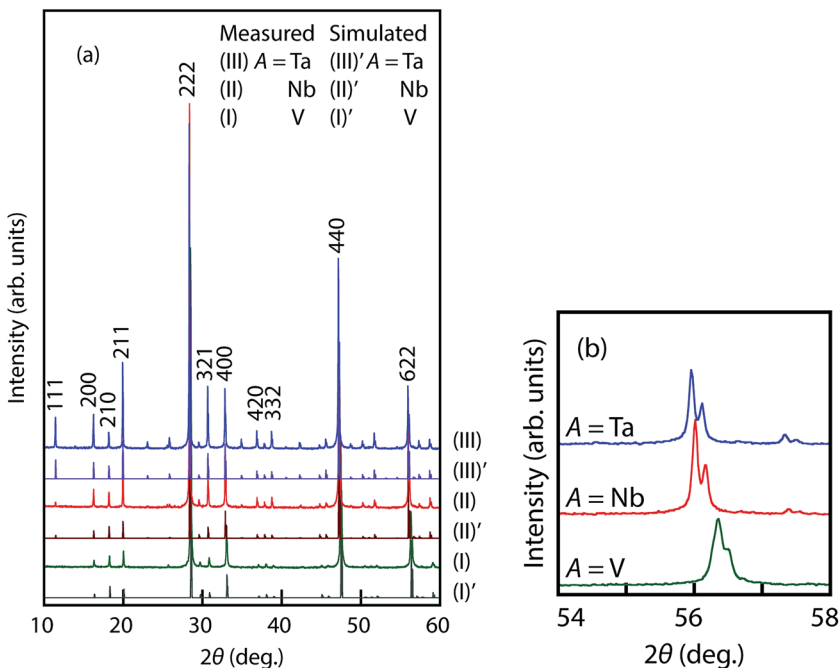


Fig. 3 (a) Powder X-ray diffraction (XRD) patterns for the sintered compacts of  $\text{Cu}_{26}\text{A}_2\text{Sn}_6\text{S}_{32}$  ( $\text{A} = \text{V}, \text{Nb}, \text{Ta}$ ) denoted by (I), (II), and (III) with simulated ones denoted by (I)', (II)', and (III)', respectively, over the  $2\theta$  range of  $10^\circ$  to  $60^\circ$ . The major peaks are labeled with Miller indices  $hkl$ . (b) The 622 peaks on the expanded scale.

Table 1 Lattice parameters refined for the as-prepared ingots ( $a_1, a_2$ ) and the hot-press sintered compacts (a) of  $\text{Cu}_{26}\text{A}_2\text{Sn}_6\text{S}_{32}$  ( $\text{A} = \text{V}, \text{Nb}, \text{Ta}$ )

| Nominal composition                                 | Lattice parameter |                  |          |
|---|-------------------|------------------|----------|
|   | As-prepared ingot | Sintered compact |          |
|   | $a_1$ (nm)        | $a_2$ (nm)       | $a$ (nm) |
| $\text{Cu}_{26}\text{V}_2\text{Sn}_6\text{S}_{32}$  | 1.0798            | 1.0759           | 1.0812   |
| $\text{Cu}_{26}\text{Nb}_2\text{Sn}_6\text{S}_{32}$ | 1.0852            | 1.0810           | 1.0877   |
| $\text{Cu}_{26}\text{Ta}_2\text{Sn}_6\text{S}_{32}$ | 1.0865            | 1.0827           | 1.0885   |

Table 2. It should be noted that the measured density  $d$  is larger by  $\sim 3\%$  than the calculated one estimated from the lattice parameter  $a$  and nominal composition. This difference suggests that the actual composition deviates from the nominal one. The average values of the composition were calculated from five spots EDX data on the surface and are listed in Table 2. We calculated the composition using two assumptions: (i) the sum of the number of cations ( $\text{Cu}, \text{A}$ , and  $\text{Sn}$ ) is 34, and (ii) the number of  $\text{S}$  atoms in the unit cell is 32. The calculated density was estimated from the  $a$  and EDX composition. In the case of assumption (i), the calculated density was smaller than the measured one. For example, the calculated density of  $4.4 \text{ g cm}^{-3}$  for the  $\text{A} = \text{V}$  sintered compact is 9% lower than its measured value of  $4.73 \text{ g cm}^{-3}$  at room temperature. On the other hand, assumption (ii) provides a reasonable agreement between the calculated and measured densities for all systems. In the  $\text{A} = \text{V}$  sample, the calculated and measured densities are  $4.80 \text{ g cm}^{-3}$  and  $4.73 \text{ g cm}^{-3}$ , respectively. For all samples, the measured

densities were estimated to be greater than 96% of the calculated densities. In assumption (ii), the composition of the cations is larger than the stoichiometric one. These extra cations are a result of the loss of sulfur during the sintering process. To understand the better agreement for (ii), it should

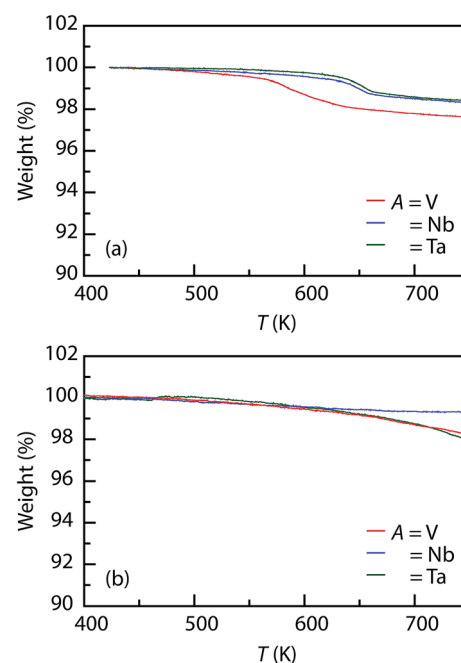


Fig. 4 Thermogravimetry curves for the powdered samples of (a) as-prepared ingots and (b) sintered compacts of  $\text{Cu}_{26}\text{A}_2\text{Sn}_6\text{S}_{32}$  ( $\text{A} = \text{V}, \text{Nb}, \text{Ta}$ ).

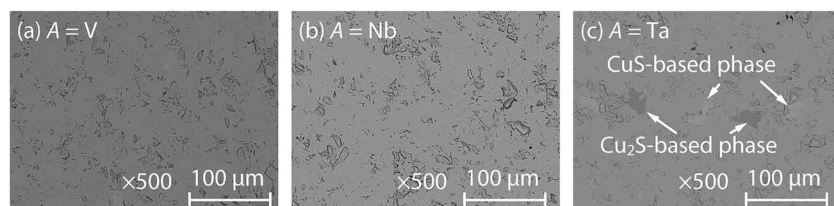


Fig. 5 Backscattered electron images of the hot-press sintered compacts of  $\text{Cu}_{26}\text{A}_2\text{Sn}_6\text{S}_{32}$  (A = (a) V, (b) Nb, (c) Ta). In (c) for A = Ta, the gray and dark gray areas are CuS- and  $\text{Cu}_2\text{S}$ -based secondary phases, respectively.

be noted that relatively large voids are present in the colusite crystal structure, such as the interstitial site 6b (0, 0, 1/2) surrounded by four S atoms as shown in Fig. 1.<sup>36,37</sup> The extra cations could occupy these large voids. For example, in the A = Ta system, the interatomic distance between the interstitial 6b site and the nearest S site is 0.2357 nm. This distance fairly agrees with the one between the Cu and S in the  $\text{CuS}_4$  tetrahedron (0.2363 nm), suggesting that the interstitial 6b site could be partially filled with extra Cu atoms.

### 3.2 Thermoelectric properties

The temperature dependences of the Seebeck coefficient  $S$  and electrical resistivity  $\rho$  for the sintered compacts of  $\text{Cu}_{26}\text{A}_2\text{Sn}_6\text{S}_{32}$  (A = V, Nb, Ta) over the temperature range of 300–670 K are shown in Fig. 6(a) and (b), respectively. Both  $\rho$  and  $S$  increase monotonically with temperature, which are the characteristics of a degenerate semiconductor. This trend is in agreement with previous studies performed on V-based colusite compounds.<sup>32–35</sup> The signs of  $S$  and Hall coefficient  $R_H$  (see Table 3) are positive, confirming p-type carrier transport. The  $\rho$

for A = Ta is lower than those for A = V and Nb over the whole temperature range measured. At 660 K, the  $\rho$  for A = V, Nb, and Ta is 63  $\mu\Omega$  m, 73  $\mu\Omega$  m, and 57  $\mu\Omega$  m, respectively. The secondary phases in the A = Ta sample probably contribute p-type charge carriers, reducing the electrical resistivity in comparison to the A = Nb and V samples. The value of  $\rho$  for A = V is lower than that for the sample  $\text{Cu}_{26}\text{V}_2\text{Sn}_6\text{S}_{32}$  reported by Suekuni *et al.*,<sup>34</sup> which reaches 110  $\mu\Omega$  m at 660 K. The former and latter sintered compacts consist of a single colusite phase and two colusite phases, respectively. Moreover, the former and latter values were measured for the actual compositions  $\text{Cu}_{26.8}\text{V}_{2.0}\text{Sn}_{5.3}\text{S}_{28.2}$  and  $\text{Cu}_{25.97}\text{V}_{2.09}\text{Sn}_{5.95}\text{S}_{30.62}$  (80%)/ $\text{Cu}_{25.15}\text{V}_{2.34}\text{Sn}_{6.51}\text{S}_{31.43}$  (20%), respectively. The differences in the crystal phases and chemical composition between two sintered compacts result in the difference in  $\rho$ . The  $S$  for A = V, Nb and Ta increases with temperature reaching a value of  $\sim$ 200  $\mu\text{V K}^{-1}$  at 660 K. The results suggest that the chemical substitution of Ta and Nb for V has little effect on the electrical properties, but the secondary phases in the sample for A = Ta affect the electrical properties. Fig. 6(c) shows the power factor ( $S^2/\rho$ ) of the  $\text{Cu}_{26}\text{A}_2\text{Sn}_6\text{S}_{32}$ . Owing to the lowest  $\rho$  for the sample

Table 2 Chemical compositions of the matrix phases and measured and calculated densities of colusite systems  $\text{Cu}_{26}\text{A}_2\text{Sn}_6\text{S}_{32}$  (A = V, Nb, Ta). The calculated density is estimated from the lattice parameter of the sintered compacts  $a$  (see Table 1) and the chemical composition

| Assumption          | Chemical composition |        |        |          | Calculated density<br>( $\text{g cm}^{-3}$ ) | Measured density<br>( $\text{g cm}^{-3}$ ) |
|---------------------|----------------------|--------|--------|----------|--|--|
|                     | Cu                   | V      | Sn     | S        |  |  |
| Nominal composition | 26                   | 2      | 6      | 32       | 4.59   | 4.73                                       |
| (i) Cations = 34    | 26.8(12)             | 2.0(2) | 5.3(3) | 28.2(11) | 4.4(2)                                       |  |
| (ii) Sulfur = 32    | 29.3(10)             | 2.2(3) | 5.8(3) | 32       | 4.8(1)                                       |  |
| Assumption          | Chemical composition |        |        |          | Calculated density<br>( $\text{g cm}^{-3}$ ) | Measured density<br>( $\text{g cm}^{-3}$ ) |
|                     | Cu                   | Nb     | Sn     | S        |  |  |
| Nominal composition | 26                   | 2      | 6      | 32       | 4.61   | 4.80                                       |
| (i) Cations = 34    | 27.0(19)             | 1.9(2) | 5.1(6) | 28.6(18) | 4.4(2)                                       |  |
| (ii) Sulfur = 32    | 30.2(13)             | 2.2(1) | 5.7(6) | 32       | 4.9(1)                                       |  |
| Assumption          | Chemical composition |        |        |          | Calculated density<br>( $\text{g cm}^{-3}$ ) | Measured density<br>( $\text{g cm}^{-3}$ ) |
|                     | Cu                   | Ta     | Sn     | S        |  |  |
| Nominal composition | 26                   | 2      | 6      | 32       | 4.83   | 5.03                                       |
| (i) Cations = 34    | 26.3(14)             | 2.3(4) | 5.4(4) | 29.2(15) | 4.7(2)                                       |  |
| (ii) Sulfur = 32    | 28.8(13)             | 2.6(5) | 5.9(4) | 32       | 5.2(2)                                       |  |



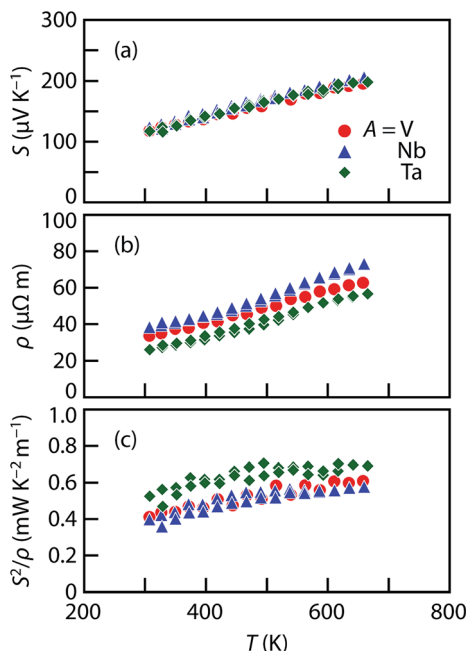


Fig. 6 Temperature dependence of (a) Seebeck coefficient  $S$ , (b) electrical resistivity  $\rho$ , and (c) thermoelectric power factor  $S^2/\rho$  for the sintered compacts of  $\text{Cu}_{26}\text{A}_2\text{Sn}_6\text{S}_{32}$  ( $\text{A} = \text{V}, \text{Nb}, \text{Ta}$ ) over the temperature range of 300–670 K. The  $S$  and  $\rho$  were measured during both heating and cooling cycles.

Table 3 Hall coefficient  $R_H$ , carrier concentration  $p$ , hole mobility  $\mu$ , and effective mass  $m^*$  at room temperature for the sintered compacts of  $\text{Cu}_{26}\text{A}_2\text{Sn}_6\text{S}_{32}$  ( $\text{A} = \text{V}, \text{Nb}, \text{Ta}$ ), where  $m_0$  is the free electron mass

| Nominal composition                                 | $R_H$ ( $10^{-8} \text{ m}^3 \text{ C}^{-1}$ ) | $p$ ( $10^{20} \text{ cm}^{-3}$ ) | $\mu$ ( $\text{cm}^2 \text{ V}^{-1} \text{ s}^{-1}$ ) | $m^*/m_0$ |
|---|--|-----------------------------------|---|-----------|
| $\text{Cu}_{26}\text{V}_2\text{Sn}_6\text{S}_{32}$  | 1.50   | 4.2                               | 4.4   | 3.2       |
| $\text{Cu}_{26}\text{Nb}_2\text{Sn}_6\text{S}_{32}$ | 1.35   | 4.7                               | 3.5   | 3.6       |
| $\text{Cu}_{26}\text{Ta}_2\text{Sn}_6\text{S}_{32}$ | 0.95   | 6.6                               | 3.6   | 4.3       |

with  $\text{A} = \text{Ta}$ , the  $S^2/\rho$  reaches the highest value of  $\sim 0.69 \text{ mW K}^{-2} \text{ m}^{-1}$  at 660 K.

We found that  $S$  and  $\rho$  are proportional to the hole carrier concentration  $p$  using the following relations:

$$S = \frac{8\pi^2 k_B^2}{3eh^2} m^* T \left( \frac{\pi}{3p} \right)^{\frac{2}{3}} \quad (2)$$

$$\frac{1}{\rho} = p e \mu \quad (3)$$

where  $k_B$  is Boltzmann's constant,  $h$  is Planck's constant,  $e$  is the electronic charge and  $\mu$  is the electrical mobility. They are derived from the parabolic band model with acoustic phonon scattering assumption for degenerate semiconductors.<sup>6,42</sup> The  $p$  was estimated from the formula  $p = 1/eR_H$ , where  $e$  represents the electronic charge and  $R_H$  is the Hall coefficient measured at room temperature. The values of  $p$  listed in Table 3 for all samples are in the range from  $4.2 \times 10^{20} \text{ cm}^{-3}$  to  $6.6 \times$

$10^{20} \text{ cm}^{-3}$ , which fall in the range expected for degenerate semiconductors. Similar values have been reported for synthetic colusites.<sup>34</sup> The value of  $p$  ( $\sim 6.6 \times 10^{20} \text{ cm}^{-3}$ ) for  $\text{Cu}_{26}\text{Ta}_2\text{Sn}_6\text{S}_{32}$  is slightly higher than those for  $\text{Cu}_{26}\text{Nb}_2\text{Sn}_6\text{S}_{32}$  ( $4.7 \times 10^{20} \text{ cm}^{-3}$ ) and  $\text{Cu}_{26}\text{V}_2\text{Sn}_6\text{S}_{32}$  ( $\sim 4.2 \times 10^{20} \text{ cm}^{-3}$ ).  $\rho$  is proportional to  $1/p$  (eqn (3)); therefore, the  $\rho$  for  $\text{A} = \text{Ta}$  is lower than those for  $\text{A} = \text{V}$  and  $\text{Nb}$ . The SEM-EDX investigations reveal the formation of  $\text{CuS}$ - and  $\text{Cu}_2\text{S}$ -based secondary phases in  $\text{Cu}_{26}\text{Ta}_2\text{Sn}_6\text{S}_{32}$ , indicating that the chemical composition of the colusite matrix deviates from the nominal one. The presence of secondary phases in the  $\text{A} = \text{Ta}$  sample contributes p-type charge carriers, leading to a lower  $\rho$  and higher  $S^2/\rho$ .

The hole mobility  $\mu$  (Table 3) of  $\text{Cu}_{26}\text{A}_2\text{Sn}_6\text{S}_{32}$  with  $\text{A} = \text{V}, \text{Nb}$ , and  $\text{Ta}$  is estimated to be  $\sim 4.4 \text{ cm}^2 \text{ V}^{-1} \text{ s}^{-1}$ ,  $\sim 3.5 \text{ cm}^2 \text{ V}^{-1} \text{ s}^{-1}$ , and  $\sim 3.6 \text{ cm}^2 \text{ V}^{-1} \text{ s}^{-1}$ , respectively. The similar values of the  $\mu$  suggest that the microstructures of the  $\text{CuS}$ - and  $\text{Cu}_2\text{S}$ -based secondary phases have only a small effect on the  $\mu$  of the systems. As already reported in a previous study,<sup>34</sup> the  $p$  for Sn-poor sintered compacts ( $\text{Cu}_{26}\text{V}_2\text{Sn}_{6-x}\text{S}_{32}$ ,  $x = 0.5, 1.0$ ) is higher than that for  $x = 0$ , leading to a higher  $S^2/\rho$ . Consequently, a fine-tuning of the  $p$  by changing the Sn content would further boost the  $S^2/\rho$  of the  $\text{A} = \text{Nb}$  and  $\text{Ta}$  systems.

The room-temperature values of  $m^*$  were calculated from measured  $S$  and  $\rho$  and are given in Table 3. For the three samples, the values of  $m^*$  lie in the range of  $3.2m_0$  to  $4.3m_0$  ( $m_0$  is the free electron mass). From the relation of  $S \propto m^*$  in eqn (2), the heavy  $m^*$  should lead to a high  $S$  for the systems. The Mahan-Sofo theory shows that a local increase of DOS at the Fermi energy results in an increase of the  $m^*$ , enhancing the  $S$ .<sup>43,44</sup>  $S$  is proportional to  $m^*$  and  $(1/p)^{2/3}$  (eqn (2)). The differences in  $m^*$  and  $(1/p)^{2/3}$  between the sintered compacts of  $\text{A} = \text{V}$ ,  $\text{Nb}$ , and  $\text{Ta}$  result in almost the same values of  $S$  for all the samples.

The temperature dependences of the total thermal conductivity  $\kappa_{\text{total}}$  and lattice thermal conductivity  $\kappa_{\text{latt}}$  for the sintered compacts of  $\text{Cu}_{26}\text{A}_2\text{Sn}_6\text{S}_{32}$  ( $\text{A} = \text{V}, \text{Nb}, \text{Ta}$ ) are shown in Fig. 7. The electronic thermal conductivity  $\kappa_{\text{el}}$  was estimated using the Wiedemann-Franz relation ( $\kappa_{\text{el}} = LT/\rho$ ), where  $L$  is the Lorenz number. Then the  $\kappa_{\text{latt}}$  was calculated by subtracting  $\kappa_{\text{el}}$  from  $\kappa_{\text{total}}$ . In a single parabolic band dominated by acoustic phonon scattering,  $L$  can be estimated as a function of reduced chemical potential ( $\zeta^*$ ).<sup>15,45–47</sup>

$$L = \left( \frac{k_B}{e} \right)^2 \frac{3F_0(\zeta^*)F_2(\zeta^*) - F_2(\zeta^*)^2}{F_0(\zeta^*)^2} \quad (4)$$

$\zeta^*$  was obtained from the experimental  $S$  values using the following equation:

$$S = \frac{k_B}{e} \left( \frac{2F_1(\zeta^*)}{F_0(\zeta^*)} - \zeta^* \right) \quad (5)$$

The Fermi integrals  $F_m(\zeta^*)$  are defined as:

$$F_m(\zeta^*) = \int_0^\infty \frac{x^m}{1 + \exp(x - \zeta^*)} dx \quad (6)$$

where  $x$  is the reduced energy of carriers. The temperature dependence of the estimated  $L$  is given in Fig. S3 in the ESI.† For example, the  $L$  at 660 K of  $\text{A} = \text{V}, \text{Nb}$  and  $\text{Ta}$  is  $\sim 1.6 \times 10^{-8}$



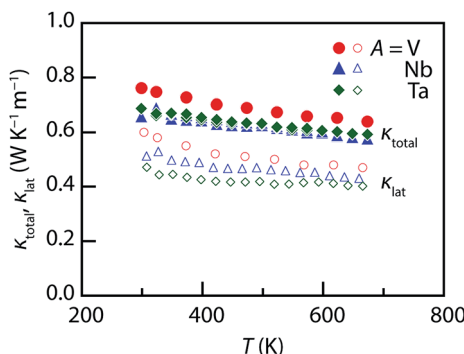


Fig. 7 Temperature dependence of the total thermal conductivity  $\kappa_{\text{total}}$  and its lattice contribution  $\kappa_{\text{lat}}$  for the sintered compacts of  $\text{Cu}_{26}\text{A}_2\text{Sn}_6\text{S}_{32}$  ( $\text{A} = \text{V}, \text{Nb}, \text{Ta}$ ) on heating and cooling cycles over the temperature range of 300–670 K.

$\text{W}\Omega\text{K}^{-2}$ . This procedure can be applied since colusites exhibit a degenerate semiconducting-like behavior. The chemical substitution of Ta and Nb for V has little effect on the thermal transport as in the electrical transport. The complex unit cell of colusite systems yields very low  $\kappa_{\text{lat}}$  values below  $0.6\text{ W K}^{-1}\text{ m}^{-1}$ , which gradually decrease with increasing temperature. This is consistent with the previous results on  $\text{A} = \text{V}$ .<sup>33,34</sup> The lowest  $\kappa_{\text{lat}}$  for the  $\text{A} = \text{Ta}$  sample would be provided by the strain and/or defect in the crystal structure induced by the secondary phases, which scatter effectively the heat-carrying phonons. The sintered compact of  $\text{Cu}_{26}\text{Ta}_2\text{Sn}_6\text{S}_{32}$  shows the lowest  $\kappa_{\text{lat}}$ ; for example, at 670 K the  $\kappa_{\text{lat}}$  of the  $\text{A} = \text{V}, \text{Nb}, \text{Ta}$  systems is  $\sim 0.47\text{ W K}^{-1}\text{ m}^{-1}$ ,  $\sim 0.43\text{ W K}^{-1}\text{ m}^{-1}$ , and  $\sim 0.40\text{ W K}^{-1}\text{ m}^{-1}$ , respectively. The very low value of  $\kappa_{\text{lat}}$  is of great advantage to further develop high-performance thermoelectric materials.

Fig. 8 shows the dimensionless thermoelectric figure of merit  $ZT$  versus temperature. The  $ZT$  for the  $\text{A} = \text{V}$  and Nb samples monotonically increases with temperature and achieves a value of 0.6–0.7 at 670 K. Comparable values were obtained by Suekuni *et al.* for  $\text{Cu}_{26}\text{V}_2\text{E}_6\text{S}_{32}$  ( $\text{E} = \text{Sn}, \text{Ge}$ ), with a  $ZT$  of 0.6 and 0.7 at 663 K for  $\text{Cu}_{26}\text{V}_2\text{Sn}_6\text{S}_{32}$  and  $\text{Cu}_{26}\text{V}_2\text{Ge}_6\text{S}_{32}$ , respectively.<sup>33</sup> Due to the lower  $\rho$  and  $\kappa_{\text{total}}$ , the  $\text{A} = \text{Ta}$  sample reaches a higher value of 0.8 at 670 K. This value approaches the

thermoelectric performances of tetrahedrite compounds at the same temperature ( $ZT \sim 1.0$ ).<sup>27</sup> We have successfully demonstrated the promising  $ZT$  for environmentally friendly colusites  $\text{Cu}_{26}\text{A}_2\text{Sn}_6\text{S}_{32}$  ( $\text{A} = \text{Nb}, \text{Ta}$ ) at intermediate temperature ( $\sim 700\text{ K}$ ).

## 4. Conclusion

We have successfully developed a new class of environmentally friendly and cost-effective thermoelectric materials based on colusites  $\text{Cu}_{26}\text{A}_2\text{Sn}_6\text{S}_{32}$  ( $\text{A} = \text{Nb}, \text{Ta}$ ). The as-prepared ingots consist of two colusite phases with different lattice parameters, which have been converted to single-phase samples by hot-press sintering. The chemical substitution of isoelectronic Nb and Ta for V has little effect on the thermoelectric properties. For the three systems, the heavy effective mass ( $3m_0$ – $4m_0$ ) leads to a high power factor. Furthermore, the complex unit cell of colusite yields very low lattice thermal conductivity below  $0.6\text{ W K}^{-1}\text{ m}^{-1}$  over the temperature range of 300–670 K. For the  $\text{A} = \text{Ta}$  sample, the  $\text{CuS}$ - and  $\text{Cu}_2\text{S}$ -based secondary phases formed in the sintered compact effectively scatter the phonons, leading to a lower lattice thermal conductivity. Moreover, the carrier concentration in the system is the highest among all the samples, resulting in a higher power factor. Consequently, the  $\text{A} = \text{Ta}$  sample shows an enhanced  $ZT$  value of  $\sim 0.8$  at 670 K.

## Conflict of interest

The authors declare that they have no competing financial interests.

## Author contributions

Y. K. and Y. B. contributed equally to this work. M. O., K. S., and T. T. designed the project. Y. K., Y. B., M. O., and M. A. synthesized and sintered the samples. Y. K., Y. B., and M. O. performed the XRD, SEM, and TG experiments, and investigated the electrical and thermal properties. Y. K., Y. B., M. O., K. S., and T. T. analyzed the results. Y. K., Y. B., M. O., K. S., and T. T. drafted the manuscript. All authors read and approved the final manuscript.

## Acknowledgements

The authors are grateful to Mr Masaru Kunii of AIST and Ms Naoko Fujimoto of AIST for preparing the samples, and also Mr Hirotaka Nishiate of AIST for operating the ZEM-3, LFA 457, and Hall measurement system. This work was supported as part of the International Joint Research Program for Innovative Energy Technology funded by the Ministry of Economy, Trade and Industry, Japan. This work at AIST was supported by JSPS KAKENHI Grant Number 25420699.

## References

- 1 *Science & Technology Review*, Lawrence Livermore National Laboratory, September, 2009, pp. 17–19.

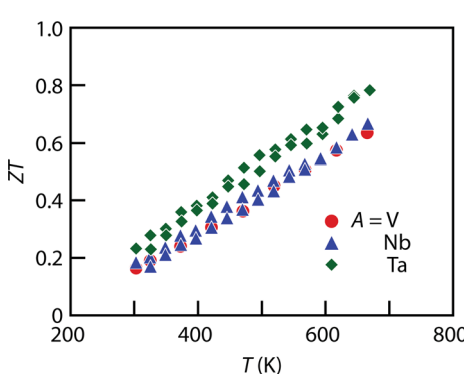


Fig. 8 Temperature dependence of the thermoelectric figure of merit  $ZT$  for  $\text{Cu}_{26}\text{A}_2\text{Sn}_6\text{S}_{32}$  ( $\text{A} = \text{V}, \text{Nb}, \text{Ta}$ ) sintered compacts over the temperature range of 300–670 K during heating and cooling cycles.



2 T. Kajikawa, in *Thermoelectrics Handbook: Macro to Nano*, ed. D. M. Rowe, CRC Press, Boca Raton, 2005, p. 50-1.

3 L. E. Bell, *Science*, 2008, **321**, 1457–1461.

4 D. M. Rowe, in *Thermoelectrics and its Energy Harvesting: Modules, Systems, and Applications in Thermoelectrics*, ed. D. M. Rowe, CRC Press, Boca Raton, 2012, p. 23-1.

5 J. Yang, in *Thermoelectrics and its Energy Harvesting: Modules, Systems, and Applications in Thermoelectrics*, ed. D. M. Rowe, CRC Press, Boca Raton, 2012, p. 25-1.

6 G. J. Snyder and E. S. Toberer, *Nat. Mater.*, 2008, **7**, 105–114.

7 J. R. Sootsman, D. Y. Chung and M. G. Kanatzidis, *Angew. Chem., Int. Ed.*, 2009, **48**, 8616–8639.

8 M. G. Kanatzidis, *Chem. Mater.*, 2010, **22**, 648–659.

9 C. J. Vineis, A. Shakouri, A. Majumdar and M. G. Kanatzidis, *Adv. Mater.*, 2010, **22**, 3970–3980.

10 K. Nielsch, J. Bachmann, J. Kimling and H. Böttner, *Adv. Energy Mater.*, 2011, **1**, 713–731.

11 M. Ohta, K. Biswas, S.-H. Lo, J. Q. He, D. Y. Chung, V. P. Dravid and M. G. Kanatzidis, *Adv. Energy Mater.*, 2012, **2**, 1117–1123.

12 K. Biswas, J. Q. He, I. D. Blum, C.-I. Wu, T. P. Hogan, D. N. Seidman, V. P. Dravid and M. G. Kanatzidis, *Nature*, 2012, **489**, 414–418.

13 L.-D. Zhao, V. P. Dravid and M. G. Kanatzidis, *Energy Environ. Sci.*, 2014, **7**, 251–268.

14 P. Jood, M. Ohta, M. Kunii, X. K. Hu, H. Nishiate, A. Yamamoto and M. G. Kanatzidis, *J. Mater. Chem. C*, 2015, **3**, 10401–10408.

15 X. K. Hu, P. Jood, M. Ohta, M. Kunii, K. Nagase, H. Nishiate, M. G. Kanatzidis and A. Yamamoto, *Energy Environ. Sci.*, 2016, **9**, 517–529.

16 L.-D. Zhao, S.-H. Lo, Y. S. Zhang, H. Sun, G. J. Tan, C. Uher, C. Wolverton, V. P. Dravid and M. G. Kanatzidis, *Nature*, 2014, **508**, 373–377.

17 L.-D. Zhao, G. J. Tan, S. Q. Hao, J. Q. He, Y. L. Pei, H. Chi, H. Wang, S. K. Gong, H. B. Xu, V. P. Dravid, C. Uher, G. J. Snyder, C. Wolverton and M. G. Kanatzidis, *Science*, 2016, **351**, 141–144.

18 D. Kraemer, J. Sui, K. McEnaney, H. Zhao, Q. Jie, Z. F. Ren and G. Chen, *Energy Environ. Sci.*, 2015, **8**, 1299–1308.

19 K. Suekuni and T. Takabatake, *APL Mater.*, 2016, **4**, 104503.

20 Y. He, T. Day, T. S. Zhang, H. L. Liu, X. Shi, L. D. Chen and G. J. Snyder, *Adv. Mater.*, 2014, **26**, 3974–3978.

21 L. L. Zhao, X. L. Wang, F. Y. Fei, J. Y. Wang, Z. X. Cheng, S. X. Dou, J. Wang and G. J. Snyder, *J. Mater. Chem. A*, 2015, **3**, 9432–9437.

22 G. Dennler, R. Chmielowski, S. Jacob, F. Capet, P. Roussel, S. Zastrow, K. Nielsch, I. Opahle and G. K. H. Madsen, *Adv. Energy Mater.*, 2014, **4**, 1301581.

23 K. Suekuni, K. Tsuruta, M. Kunii, H. Nishiate, E. Nishibori, S. Maki, M. Ohta, A. Yamamoto and M. Koyano, *J. Appl. Phys.*, 2013, **113**, 043712.

24 X. Lu, D. T. Morelli, Y. Xia, F. Zhou, V. Ozolins, H. Chi, X. Y. Zhou and C. Uher, *Adv. Energy Mater.*, 2013, **3**, 342–348.

25 X. Lu and D. T. Morelli, *MRS Commun.*, 2013, **3**, 129–133.

26 J. Heo, G. Laurita, S. Muir, M. A. Subramanian and D. A. Keszler, *Chem. Mater.*, 2014, **26**, 2047–2051.

27 X. Lu, D. T. Morelli, Y. Xia and V. Ozolins, *Chem. Mater.*, 2015, **27**, 408–413.

28 Y. Bouyrie, C. Candolfi, V. Ohorodniichuk, B. Malaman, A. Dauscher, J. Tobola and B. Lenoir, *J. Mater. Chem. C*, 2015, **3**, 10476–10487.

29 R. Chetty, A. Bali and R. C. Mallik, *J. Mater. Chem. C*, 2015, **3**, 12364–12378.

30 R. Chetty, A. Bali, M. H. Naik, G. Rogl, P. Rogl, M. Jain, S. Suwas and R. C. Mallik, *Acta Mater.*, 2015, **100**, 266–274.

31 P. Jood and M. Ohta, *Materials*, 2015, **8**, 1124–1149.

32 K. Suekuni, F. S. Kim and T. Takabatake, *J. Appl. Phys.*, 2014, **116**, 063706.

33 K. Suekuni, F. S. Kim, H. Nishiate, M. Ohta, H. I. Tanaka and T. Takabatake, *Appl. Phys. Lett.*, 2014, **105**, 132107.

34 F. S. Kim, K. Suekuni, H. Nishiate, M. Ohta, H. I. Tanaka and T. Takabatake, *J. Appl. Phys.*, 2016, **119**, 175105.

35 C. Bourgès, M. Gilmas, P. Lemoine, N. E. Mordvinov, O. I. Lebedev, E. Hug, V. Nassif, B. Malaman, R. Daou and E. Guilmeau, *J. Mater. Chem. C*, 2016, **4**, 7455–7463.

36 P. G. Spry, S. Merlini, S. Wang, X. M. Zhang and P. R. Buseck, *Am. Mineral.*, 1994, **79**, 750–762.

37 O. V. Frank-Kamenetskaya, I. V. Rozhdestvenskaya and L. A. Yanulova, *J. Struct. Chem.*, 2002, **43**, 89–100.

38 H. Wyers, *Br. J. Ind. Med.*, 1946, **3**, 177–182.

39 J. L. Domingo, *Reprod. Toxicol.*, 1996, **10**, 175–182.

40 V. Petricek, M. Dusek and L. Palatinus, *Z. Kristallogr.*, 2014, **229**, 345–352.

41 K. Momma and F. Izumi, *J. Appl. Crystallogr.*, 2011, **44**, 1272–1276.

42 M. Cutler, J. F. Leavy and R. L. Fitzpatrick, *Phys. Rev.*, 1964, **133**, A1143–A1152.

43 G. D. Mahan and J. O. Sofo, *Proc. Natl. Acad. Sci. U. S. A.*, 1996, **93**, 7436–7439.

44 J. P. Heremans, V. Jovovic, E. S. Toberer, A. Saramat, K. Kurosaki, A. Charoenphakdee, S. Yamanaka and G. J. Snyder, *Science*, 2008, **321**, 554–557.

45 A. F. May, J.-P. Fleurial and G. J. Snyder, *Phys. Rev. B: Condens. Matter Mater. Phys.*, 2008, **78**, 125205.

46 S. Johnsen, J. Q. He, J. Androulakis, V. P. Dravid, I. Todorov, D. Y. Chung and M. G. Kanatzidis, *J. Am. Chem. Soc.*, 2011, **133**, 3460–3470.

47 M. Ohta, S. Satoh, T. Kuzuya, S. Hirai, M. Kunii and A. Yamamoto, *Acta Mater.*, 2012, **60**, 7232–7240.

